RADIO EMISSION FROM ISOLATED PROTOSTARS

Erum Y. Vohra [1], ADVISOR: Jonathan C. Tan [1,2], Viviana Rosero [3], Joshua Marvil [4], Francisco Sequeira Murillo [5] and Kei E. I. Tanaka [6]

[1] Department of Astronomy, University of Virginia, Charlottesville, Virginia 22904, USA
[2] Department of Space, Earth & Environment, Chalmers University of Technology, SE-412 93 Gothenburg, Sweden
[3] Department of Astronomy, California Institute of Technology, Pasadena, California 91125, USA
[4] National Radio Astronomy Observatory, 1003 Lópezville Rd., Socorro, NM 87801, USA
[5] Department of Astronomy, University of Wisconsion-Madison, Madison 53706, Wisconsin, USA
[6] Department of Earth and Planetary Sciences, Tokyo Institute of Technology, Meguro, Tokyo 152-8551, Japan

ABSTRACT

The formation of massive stars is an important process, but with many open questions, especially the role of the surrounding protocluster environment. We analyze multiwavelength Very Large Array (VLA) radio continuum observations for eleven intermediate and high-mass protostars from the SOFIA Massive (SOMA) Star Formation Survey, which appear to be relatively isolated in their mid to far-infrared morphology. However, in the radio continuum, these regions appear to have some multiplicity. The centimeter continuum emission highlights ionized gas and we examine the morphology and spectral index of each protostar to determine the nature of the ionization process. We constrain the ionizing luminosity of the protostars and discuss these results in relation to extended spectral energy distributions (E-SEDs) of the protostars from the radio to the mid-infrared. We examine how our sample of eleven protostars compares to the larger SOMA sample of about fifty sources, presenting our results in a radio luminosity vs. bolometric luminosity sequence that demonstrates that the formation mechanisms of high and low-mass protostars may be linked.

1. INTRODUCTION

The mechanism which drives the formation of high mass stars is still actively debated. Traditional models propose a scaled-up version of core accretion, while others posit a more competitive accretion model unique to intermediate and high mass stars.

The SOFIA Massive (SOMA) Star Formation Survey aims to characterize a large sample of high and intermediate mass protostars across a range of environments, masses, and evolutionary stages, using data from SOFIA-FORECAST. In Paper I (De Buizer et al. 2017), the first eight sources were presented. Paper II (Liu et al. 2019) focused on sources with high luminosity, while Paper III (Liu et al. 2020) presented intermediate mass sources. Paper IV (Fedriani et al. 2022) presented several isolated sources.

However, modeling radiative transfer (Zhang & Tan 2018) with only infrared data created degeneracies in fitting key parameters. Incorporating data from the centimeter continuum, along with models for free-free emission as in Tanaka et al. (2016), provides a more comprehensive overview of the object and resolves degeneracies. This is the motivation for conducting follow-up observations in centimeter continuum. Rosero et al. (2019a) accompanies the De Buizer et al. (2017), while two papers by Sequeira-Murillo et al. (In Prep) accompany Papers II and III.

This study is the fourth in a series of papers that supplement and expand on the SOMA survey. Our goal is to build a more comprehensive sample by using radio observations to analyze each region and construct extended spectral energy distributions (E-SEDs). This paper presents high sensitivity data from the VLA at 1.3 and 6 cm for ten sources. Our approach follows that of the previous Radio SOMA papers: we reduce the centimeter continuum, measure fluxes, and analyze morphology and multiplicity, ensuring all of the protostars are analyzed in a systematic manner.

The methodology and information about the observations are presented in Section 2. The observational results for each source are presented in Section 3, while the analysis and discussion are presented in 4. Conclusions are presented in 5.

2. METHODS

The SOMA Star Formation Survey is composed of observations from SOFIA-FORECAST. The sample presented in this paper is presented in Fedriani et al.

(2022), except for G33.92+0.11, which requires extra analysis. We present ten protostars: AFGL 2591, G25.40-0.14, G30.59-0.04, G32.03+0.05, G32.03+0.05N, G40.62-0.14, IRAS 00259+5625, IRAS 00420+5530, IRAS 23385+6053, and HH288. These sources are summarized in 1. The distances to the regions and the bolometric luminosity, presented in Columns 7 and 8, are drawn from Fedriani et al. (2022).

Table 1. SOMA IV Sources

Region	Frequency Band	R.A	Decl.	Beam Size	RMS	D[a]	L[b]
	(GHz)	(J2000)	(J2000)	($''$ x $''$, degree)	(μJy beam^{-1})	(kpc)	(10^4 $L_\odot$)
AFGL 2591	4.0 − 8.0	20 29 24.8916	+40 11 19.388	0.60 × 0.29, 74.9	12.0	3.3	20.0 − 66.0
	18.0 − 26.5	...	...	0.45 × 0.27, − 73.5	9.8	...	...
G25.40-0.14	4.0 − 8.0	18 38 08.2700	− 06 45 57.820	0.38 × 0.29, 13.1	61.0	5.7	29.0 − 84.0
	18.0 − 26.5	...	...	0.33 × 0.25, − 2.67	95.0	...	...
G30.59-0.04	4.0 − 8.0	18 47 18.9000	− 02 06 17.600	0.37 × 0.29, 7.02	31.0	11.8	21.0 − 31.0
	18.0 − 26.5	...	...	0.32 × 0.25, − 21.5	17.0	...	...
G32.03+0.05	4.0 − 8.0	18 49 37.0520	− 00 46 50.150	0.38 × 0.29, 19.9	4.5	5.5	2.0 − 120.0
	18.0 − 26.5	...	...	0.43 × 0.25, − 43.0	8.4	...	...
G32.03+0.05N	4.0 − 8.0	18 49 36.55	− 00 45 42.40	0.38 × 0.29, 19.9	5.0	5.5	4.0 − 200.0
	18.0 − 26.5	...	...	0.43 × 0.25, − 43.0	8.7	...	...
G40.62-0.14	4.0 − 8.0	19 06 01.6000	+06 46 36.200	0.32 × 0.29, 3.89	4.4	2.2	1.0 − 8.8
	18.0 − 26.5	...	...	0.39 × 0.30, − 28.6	9.0	...	...
IRAS 00259+5625	4.0 − 8.0	00 28 42.6000	+56 42 01.110	0.70 × 0.27, 63.4	5.8	2.5	0.009 − 1.1
	18.0 − 26.5	...	...	0.40 × 0.25, − 75.0	6.5	...	...
IRAS 00420+5530	4.0 − 8.0	00 44 58.5842	+55 46 45.675	0.54 × 0.28, 75.3	4.4	2.2	0.039 − 0.19
	18.0 − 26.5	...	...	0.39 × 0.25, − 70.34	6.5	...	...
IRAS 23385+6053	4.0 − 8.0	23 40 54.5171	+61 10 27.768	0.71 × 0.28, 62.7	5.5	4.9	0.10 − 0.30
	18.0 − 26.5	...	...	0.36 × 0.25, − 74.7	8.2	...	...
HH288	4.0 − 8.0	00 37 13.2580	+64 04 15.020	0.55 × 0.26, 78.0	7.0	2.0	0.02 − 0.19
	18.0 − 26.5	...	...	0.43 × 0.24, − 86.6	7.4	...	...

NOTE— Units of R.A. are hours, minutes, and seconds. Units of decl. are degrees, arcminutes, and arcseconds.
[a] References cited in Fedriani et al. (2023).
[b] Range of bolometric luminosities from the best models reported in Fedriani et al. (2023).

2.1. *VLA Data*

2.1.1. *6 cm Data*

The 6 cm (C-Band) observations for all regions consisted of two 1 GHz wide basebands centered at 5.3 and 6.3 GHz. Each of these basebands collected data in 16 unique SPWs, each comprised of 64 channels that are 2 MHz wide. The total bandwidth was 2048 MHz.

The images for each source were made with the *tclean* task in CASA and Briggs *Robust* = 0.5 weighting. We made two images for each region, each of a ∼1 GHz baseband containing 16 SPWs, and a combined image containing 32 SPWs. All of the images were primary-beam corrected and the size and position angle of the synthesized beam is recorded in Column 5 of Table 1. The rms associated with the combined image is Column 6 of Table 1. For further detail about the data reduction process, refer to Rosero et al. (2019a).

2.1.2. *1.3 cm Data*

The 1.3 cm (K-Band) observations consisted of two 4 GHz wide basebands centered at 19.9 and 23.9 GHz. Each of these basebands collected data in 32 SPWs, each compromised of 128 channels that are 1 GHz wide. The total bandwidth was 8192 MHz.

The data reduction was conducted in the same manner as that for the 6 cm observations. We made two images for each region, each of a ∼4 GHz baseband containing 32 SPWs, and a combined image containing all 64 SPWs. All of the images were primary-beam corrected and the size and position angle of the synthesized beam are recorded in Table 1.

3. RESULTS

We define a radio detection as when the peak intensity I_ν is ≥ 5 times the image rms (σ) in either of the baseband-combined images. For regions where there are no detections, we report a 3σ value for the flux density at the given frequency.

For the SOMA and *Intermediate* scales, we use the task *imstat* in CASA. For the *Inner* scale, we use *imfit* for sources with circular geometry and *imstat* for sources with more complicated geometries. Parameters were measured for the following scales: SOMA, *Intermediate*, and *Inner*. The SOMA scale refers to the aperture defined by Fedriani et al. (2022). The *Intermediate* scale is introduced as needed, for detections that appear to have a jet-like morphology or other interesting structures, like the spiral structure exhibited by G25.40-0.14. The *Inner* scale is defined by the central radio detection, which is likely associated with the protostar. For a more detailed discussion of the analysis conducted, please refer to Rosero et al. (2019a).

3.1. *Morphology and Multiplicity*

All of the regions in this paper have been detected in the centimeter continuum. We describe their morphology as compact if the detection shows no structure on the scale of a few synthesized beams, or extended otherwise. Below, we describe the centimeter wavelength detections and give a brief background. For a detailed background on these regions, see Fedriani et al. (2022).

3.1.1. *AFGL 2591*

AFGL 2591 is a region located at 3.3 kpc with several radio detections in the region (Rygl et al. 2012). We report five radio detections, all of which have been reported in the literature before (Trinidad et al. 2003). The central detection has been identified as a high-mass protostar, while the other detections are classified as HII regions (Johnston et al. 2013; Gieser et al. 2019). AFGL 2591 drives a molecular outflow oriented in the east-west direction Preibisch et al. (2003).

3.1.2. *G25.40-0.14*

G25.40-0.14 is a UC HII region with a core halo structure located at 5.7 kpc (Garay et al. 1993; Zhu et al. 2011; Ai et al. 2013). The cole halo structure is present in the centimeter continuum, exhibiting a spiral like structure around a central region with four detections. In addition, we report an additional detection of a source to the southeast, removed from the central region. Ai et al. (2013) estimates a bolometric luminosity of $10^{5.6} L_\odot$, which corresponds to a zero-age main-sequence star (ZAMS).

3.1.3. *G30.59-0.04*

Located at 11.8 kpc (Urquhart et al. 2017; Mège et al. 2021), G30.59-0.04 has been previously detected by the VLA (Fish et al. 2003). Hill et al. (2008) estimated that the clump has an upper limit of 1200 $M_\odot$ and Fedriani et al. (2022) further estimate a luminosity of $3.5{\times}10^5 L_\odot$. Our observations display three distinct, approximately spherical detections in both bands. We see some extended emission towards the southeast, which is more prominent in the 6 cm.

3.1.4. *G32.03+0.05*

G32.03+0.05, a region located at 5.5 kpc, has been previously detected several times in the radio (Becker et al. 1994). During NH_3 observations of the IRDC G32.02+0.06, Battersby et al. (2014) identified two seperate clumps, which they labeled active and quiescent. G32.03+0.05 is located within the active clump, which Battersby et al. (2014) estimated to have a mass of $\sim 5000 - 10,000 M_\odot$. Furthermore, they identify our source as a young UC HII region with no associated NH_3 emission. In our observations, G32.02+0.05 is an extended source. The source appears to have a smaller, compact inner shell, surrounded by extended emission pointing to the north. This structure is present in both bands, but the extent of the extended emission is larger in the 6 cm.

3.1.5. *G32.03+0.05N*

This source, located to the north of G32.03+0.05, has been previously identified as a warm core complex with signatures of NH_3 emission (Battersby et al. 2014). Our observations indicate two detections in the C-Band and one in the K-Band. The difference in number of detections between bands likely corresponds to the differences in the position angle of the synthesized beam between bands. Battersby et al. (2014) estimates the core masses as $\sim 100 M_\odot$.

3.1.6. *G40.62-0.14*

This region, also known as IRAS 19035+0641, is located at 2.2 kpc (Sridharan et al. 2002). The region has an outflow oriented in the northwest-southeast direction. We report two detections and based on previous study by Rosero et al. (2019b), the detection we report to the northwest of the central source is associated with an ionized jet from a young stellar object. Rosero et al. (2019b) suggest that the central source is a UC HII region.

3.1.7. *IRAS 00259+5625*

IRAS 00259+5625, is a Bok globule located at 2.4 kpc (Launhardt & Henning 1997). However, due to the large

distance and high luminosity of the globule, Launhardt et al. (1997) estimate that star formation region is of intermediate mass, unlike most low mass Bok globules. Fuente et al. (2007) resolves the continuum source into a binary source in the millimeter, estimated their masses as 0.62 and $0.24 M_{\odot}$. The region is associated with outflows oriented to the north-south (Yun & Clemens 1994). We report one detection of IRAS 00259+5625 in the 1.3 cm, where we see a compact source.

3.1.8. *IRAS 00420+5530*

This region, also known as Mol 3, is a high-mass protostellar candidate located at 2.2 kpc (Moellenbrock et al. 2009). Molinari et al. (2002) find two millimeter continuum detections and two centimeter continuum detections. The region IRAS 00420+5530 exhibits CO emission (Zhang et al. 2005). We report one detection in each band.

3.1.9. *IRAS 23385+6053*

IRAS 23385+6053, also known as Mol 160, is a region with a protostellar cluster and two HII regions (Molinari et al. 1998, 2002). The region has been resolved to contain six cores (Cesaroni et al. 2019) and Molinari et al. (2008) finds arc-like structures in 24 μm, but the precursor is unclear. The region is associated with a northeast-southeast outflow (Wolf-Chase et al. 2012). IRAS 23385+6053 appears as a point source in the K-Band in our observations.

3.1.10. *HH288*

Located at approximately 2.0 kpc (Gueth et al. 2001), HH288 is a region associated with two bipolar flows. The larger outflow is oriented in the north-south direction, while the smaller outflow is aligned in the east-west direction (Franco-Hernández & Rodríguez 2003). The region is associated with the source IRAS 00342+6347. In the centimeter continuum, HH288 appears as a small, compact source with detections only in the K-Band.

3.2. *Radio SEDs*

Figure 1 presents the SEDs for the ten regions presented in this paper. The red data points correspond to infrared data for the SOMA apertures, as measured by Fedriani et al. (2022), and the dashed lines correspond to the best fit of the data using a power law of the form $S_{\nu} \propto \nu^{\alpha}$, where α is the spectral index at the different scales. The spectral index was calculated using the flux density of the central frequencies of the images, so α is calculated over a wide range of frequencies. The uncertainty in the spectral index was calculated with a Monte Carlo simulation that bootstrapped the flux density uncertainties. We estimated an upper limit for nondetections in the spectral index by approximating S_{ν} as 3σ. At higher frequencies, we expect that the flux densities are measuring a combination of dust and free-free emission, likely adding some systematic error to the flux measurement (Brogan et al. 2016).

4. ANALYSIS AND DISCUSSION

As a tool to understand the nature of our sources, we present Figure 2, which compares the bolometric luminosity with the radio luminosity at 5 GHz for the *Inner* scale. The bolometric luminosity is drawn from the five best models calculated in Fedriani et al. (2022). Within the plot, the yellow circles represent the radio luminosity from low mass protostars associated with ionized jets from Anglada (1995). We scale their fluxes, assuming that these sources have the canonical values for ionized jets, $\alpha = 0.6$. A power law is fit to these data, represented by $S_{\nu} d^2 = 8 \times 10^3 (L_{bol})^{0.6}$. We include UC and HC HII regions from Kurtz et al. (1994), represented with $\times$, while the solid black line is radio emission from a ZAMS in an optically thin HII region (Thompson 1984). The solid cyan line represents the emission from photoionization by a protostar in optically thin conditions (Tanaka et al. 2016).

Based on the Figure 2, we see that low and high mass protostars overlap while following the power law fit of the data (Anglada et al. 2015), indicating that these protostars likely share a formation mechanism that could be universal among stars. We notice that the sources included in this sample fall closer to the upper right corner of the plot, implying that this particular subset of the SOMA sample has a large number of evolved sources compared to the previous samples. The sources that lie close to the intersection between the dashed line and the solid cyan line could possess ionizing jets or simply have a low luminosity, due to young age.

We note that this sample of protostars exhibits more multiplicity than the previous samples in the SOMA survey, putting putting it at odds with the assessment made that these protostars are isolated using only infrared data.

5. CONCLUSIONS

We present the data from the VLA to build extended SEDs from the centimeter continuum to the infrared, testing models of massive star formation via competitive accretion processes. These results continue to demonstrate the use of centimeter emission in breaking degeneracies encountered in infrared-only analysis of protostars, allowing isolation of physical parameters like mass surface density and mass of the core.

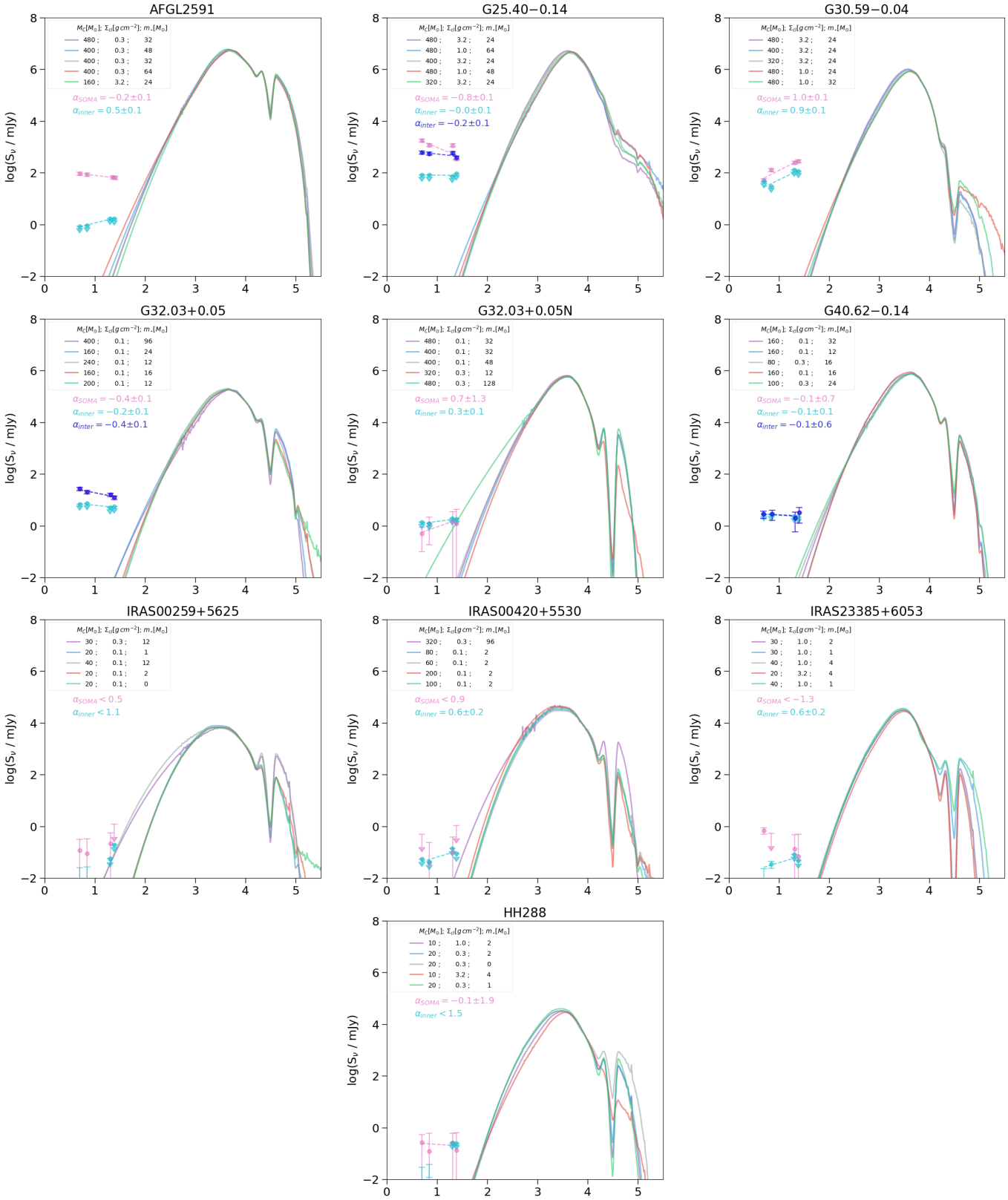

Figure 1. Radio spectral energy distributions of SOMA protostars. The data points correspond to the flux density as a function of the frequency at each scale (Pink: SOMA; Blue: *Intermediate*; Cyan: *Inner*). The dashed lines are the best fit of the radio data using a power law of the form $S_\nu \propto \nu^\alpha$. The solid lines shows the five best fits to the infrared data from the Zhang & Tan (2018) models as fit by Fedriani et al. (2022).

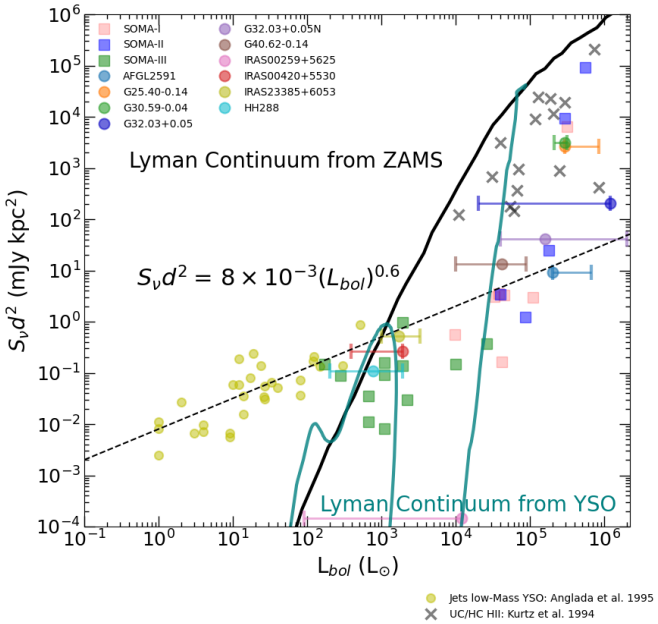

Figure 2. The radio luminosity at 5 GHz at the *Inner* scale as a function of bolometric luminosity for our ten sources. The bolometric luminosity is given by the results for the best model from Fedriani et al. (2022) and the error bars correspond to the range of luminosities for the five best models for each source. The yellow circles represent ionized jets toward low mass stars from Anglada (1995). The dashed line is a power law relation for these sources, given by Anglada et al. (2015). The × symbols are UC and HC HII regions from Kurtz et al. (1994). The solid black and the cyan lines are the radio emission expected from optically thin H II regions powered by a ZAMS star (Thompson 1984) and from a YSO (Tanaka et al. 2016), respectively.

We probed the presence of stellar multiplicity, which we note is far larger than indicated by infrared-only assessments. Further assessment is needed to draw conclusions about the nature of the multiplicity seen in these regions and what their presence may imply about the formation mechanisms of massive stars.

Facilities: VLA

Software: astropy (Astropy Collaboration et al. 2013), CASA (The CASA Team et al. 2022)

REFERENCES

Ai, M., Zhu, M., Xiao, L., & Su, H.-Q. 2013, Research in Astronomy and Astrophysics, 13, 935, doi: 10.1088/1674-4527/13/8/005

Anglada, G. 1995, in Revista Mexicana de Astronomia y Astrofisica Conference Series, Vol. 1, Revista Mexicana de Astronomia y Astrofisica Conference Series, ed. S. Lizano & J. M. Torrelles, 67

Anglada, G., Rodríguez, L. F., & Carrasco-Gonzalez, C. 2015, in Advancing Astrophysics with the Square Kilometre Array (AASKA14), 121, doi: 10.22323/1.215.0121

Astropy Collaboration, Robitaille, T. P., Tollerud, E. J., et al. 2013, A&A, 558, A33, doi: 10.1051/0004-6361/201322068

Battersby, C., Ginsburg, A., Bally, J., et al. 2014, The Astrophysical Journal, 787, 113, doi: 10.1088/0004-637X/787/2/113

Becker, R. H., White, R. L., Helfand, D. J., & Zoonematkermani, S. 1994, ApJS, 91, 347, doi: 10.1086/191941

Brogan, C. L., Hunter, T. R., Cyganowski, C. J., et al. 2016, The Astrophysical Journal, 832, 187, doi: 10.3847/0004-637X/832/2/187

Cesaroni, R., Beuther, H., Ahmadi, A., et al. 2019, A&A, 627, A68, doi: 10.1051/0004-6361/201935506

De Buizer, J. M., Liu, M., Tan, J. C., et al. 2017, The Astrophysical Journal, 843, 33, doi: 10.3847/1538-4357/aa74c8

Fedriani, R., Tan, J. C., Telkamp, Z., et al. 2022, The Astrophysical Journal, 942, 7, doi: 10.3847/1538-4357/aca4cf

Fish, V. L., Reid, M. J., Wilner, D. J., & Churchwell, E. 2003, The Astrophysical Journal, 587, 701, doi: 10.1086/368284

Franco-Hernández, R., & Rodríguez, L. F. 2003, RMxAA, 39, 107

Fuente, A., Ceccarelli, C., Neri, R., et al. 2007, A&A, 468, L37, doi: 10.1051/0004-6361:20077297

Garay, G., Rodriguez, L. F., Moran, J. M., & Churchwell, E. 1993, ApJ, 418, 368, doi: 10.1086/173396

Gieser, C., Semenov, D., Beuther, H., et al. 2019, A&A, 631, A142, doi: 10.1051/0004-6361/201935865

Gueth, F., Schilke, P., & McCaughrean, M. J. 2001, A&A, 375, 1018, doi: 10.1051/0004-6361:20010896

Hill, T., Pinte, C., Minier, V., Burton, M. G., & Cunningham, M. R. 2008, Monthly Notices of the Royal Astronomical Society, 392, 768, doi: 10.1111/j.1365-2966.2008.14103.x

Johnston, K. G., Shepherd, D. S., Robitaille, T. P., & Wood, K. 2013, A&A, 551, A43, doi: 10.1051/0004-6361/201219657

Kurtz, S., Churchwell, E., & Wood, D. O. S. 1994, ApJS, 91, 659, doi: 10.1086/191952

Launhardt, R., & Henning, T. 1997, A&A, 326, 329

Launhardt, R., Ward-Thompson, D., & Henning, T. 1997, Monthly Notices of the Royal Astronomical Society, 288, L45, doi: 10.1093/mnras/288.4.L45

Liu, M., Tan, J. C., De Buizer, J. M., et al. 2019, The Astrophysical Journal, 874, 16, doi: 10.3847/1538-4357/ab07b7

—. 2020, The Astrophysical Journal, 904, 75, doi: 10.3847/1538-4357/abbefb

Mège, P., Russeil, D., Zavagno, A., et al. 2021, A&A, 646, A74, doi: 10.1051/0004-6361/202038956

Moellenbrock, G. A., Claussen, M. J., & Goss, W. M. 2009, The Astrophysical Journal, 694, 192, doi: 10.1088/0004-637X/694/1/192

Molinari, S., Faustini, F., Testi, L., et al. 2008, A&A, 487, 1119, doi: 10.1051/0004-6361:200809821

Molinari, S., Testi, L., Brand, J., Cesaroni, R., & Palla, F. 1998, The Astrophysical Journal, 505, L39, doi: 10.1086/311591

Molinari, S., Testi, L., Rodríguez, L. F., & Zhang, Q. 2002, The Astrophysical Journal, 570, 758, doi: 10.1086/339630

Preibisch, T., Balega, Y. Y., Schertl, D., & Weigelt, G. 2003, A&A, 412, 735, doi: 10.1051/0004-6361:20031449

Rosero, V., Tanaka, K. E. I., Tan, J. C., et al. 2019a, The Astrophysical Journal, 873, 20, doi: 10.3847/1538-4357/ab0209

Rosero, V., Hofner, P., Kurtz, S., et al. 2019b, The Astrophysical Journal, 880, 99, doi: 10.3847/1538-4357/ab2595

Rygl, K. L. J., Brunthaler, A., Sanna, A., et al. 2012, A&A, 539, A79, doi: 10.1051/0004-6361/201118211

Sridharan, T. K., Beuther, H., Schilke, P., Menten, K. M., & Wyrowski, F. 2002, The Astrophysical Journal, 566, 931, doi: 10.1086/338332

Tanaka, K. E. I., Tan, J. C., & Zhang, Y. 2016, The Astrophysical Journal, 818, 52, doi: 10.3847/0004-637X/818/1/52

The CASA Team, Bean, B., Bhatnagar, S., et al. 2022, Publications of the Astronomical Society of the Pacific, 134, 114501, doi: 10.1088/1538-3873/ac9642

Thompson, R. I. 1984, ApJ, 283, 165, doi: 10.1086/162287

Trinidad, M. A., Curiel, S., Cantó, J., et al. 2003, The Astrophysical Journal, 589, 386, doi: 10.1086/374618

Urquhart, J. S., König, C., Giannetti, A., et al. 2017, Monthly Notices of the Royal Astronomical Society, 473, 1059, doi: 10.1093/mnras/stx2258

Wolf-Chase, G., Smutko, M., Sherman, R., Harper, D. A., & Medford, M. 2012, The Astrophysical Journal, 745, 116, doi: 10.1088/0004-637X/745/2/116

Yun, J. L., & Clemens, D. P. 1994, ApJS, 92, 145, doi: 10.1086/191963

Zhang, Q., Hunter, T. R., Brand, J., et al. 2005, The Astrophysical Journal, 625, 864, doi: 10.1086/429660

Zhang, Y., & Tan, J. C. 2018, The Astrophysical Journal, 853, 18, doi: 10.3847/1538-4357/aaa24a

Zhu, M., Davis, C. J., Wu, Y., et al. 2011, The Astrophysical Journal, 739, 53, doi: 10.1088/0004-637X/739/1/53